12

Autonomous Formation Flight – Design and Experiments

Yu Gu, Giampiero Campa, Brad Seanor,
Srikanth Gururajan and Marcello R. Napolitano
West Virginia University
U.S.A.

1. Introduction

Formation flight has long been performed by many species of birds for its social and aerodynamic benefits. The traditional "V" shape formation flown by birds not only helped communication between individuals, but also decreased the induced drag for each trailing bird, and thus reduced the energy required for flying (Weimerskirch et al. 2001). The benefits of formation flight have also been evaluated for manned aircraft. However, due to the high level of risk, human-piloted close formations are rarely sustained for a long enough time to fully appreciate the aerodynamic benefits. Therefore, reliable autonomous formation control can be an attractive capability for both human-piloted aircraft and Unmanned Aerial Vehicles (UAVs).

The formation control problem has been extensively discussed in recent years with numerous applications with ground mobile robots, aircraft systems, and space vehicles. In their survey paper, (Scharf et al. 2004) classified the spacecraft formation flight control algorithms into five architectures:

- *"Multiple-Input Multiple-Output, in which the formation is treated as a single multiple-input, multiple-output plan;*
- *Leader/Follower, in which individual spacecraft controllers are connected hierarchically;*
- *Virtual Structure, in which spacecraft are treated as rigid bodies embedded in an overall virtual structure;*
- *Cyclic, in which individual spacecraft controllers are connected nonhierarchically;*
- *Behavioral, in which multiple controllers for achieving different (and possibly competing) objectives are combined."*

Similar classifications can be extended to the formation control of other types of vehicles. However, due to the complexity and non-linearity associated with the aircraft dynamics, the 'leader-follower' approach was by far the most popular method for aircraft formation flight control. The advantage of the 'leader-follower' approach lies in its conceptual simplicity, where the formation flight problem is reduced to a set of tracking problems that can be analyzed and solved using standard control techniques.

In the early 1990s, a series of publications from D'Azzo and his colleagues (Dargan et al. 1992) (Buzogany et al. 1993) (Reyna et al. 1994) (Veth et al. 1995) outlined the foundation for the control of the 'leader-follower' formation flight using compensation-type controllers.

Since then, a variety of control techniques has been evaluated includeing optimal control (McCammish et al. 1996) (Dogan et al. 2005), adaptive control (Boskovic & Mehra 2003), fuzzy control (Li et al. 2005), robust control (Li et al. 2006), feedback linearization (Singh et al. 2000) (Venkataramanan & Dogan 2003), and sliding mode (Schumacher & Singh 2000). (Allen et al. 2002) performed a string stability analysis of an autonomous formation for measuring of how position errors propagate from one vehicle to another in a cascaded system. (Giulietti et al. 2000) simulated the scenario with the presence of a failure of one of the nodes, such as the loss of an aircraft.

Experimental studies for evaluating the aerodynamic effects of formation flight and for validating formation control laws have been conducted with both wind tunnel experiments (Gingras 1999) (Fowler & D'Andrea 2003) (Kutay et al. 2005) and flight-testing (Napolitano 2005) (Gu et al. 2006) (Lavretsky 2002) (Hanson et al. 2002) (How et al. 2004) (Johnson et al. 2004). Related to flight-testing efforts, the NASA Dryden Flight Research Center Autonomous Formation Flight (AFF) project in 2001 demonstrated formation control in the lateral and vertical channels with a pair of F/A-18 aircraft (Hanson et al. 2002). (How et al. 2004) at MIT performed a 2-aircraft formation flight using timing control. (Johnson et al. 2004) at Georgia Tech have been performing a series of vision-based formation flight since 2004.

This chapter presents the research effort leading to the flight demonstration of autonomous formation flight using three YF-22 research aircraft designed, built, instrumented, and tested at West Virginia University (WVU). The rest of the chapter is organized as follows. Section two presents the formation geometry and formation controller design. Section three describes the test-bed aircraft and the avionics system. The identification of the linear and nonlinear aircraft mathematical model is provided in Section four. Section five describes the formation flight simulation environment and the on-board software. Different flight-testing phases and final experimental results are presented in Section six. A brief conclusion is then provided in the final section.

2. Formation Controller Design

In the selected 'leader-follower' formation flight configuration, a Radio Control (R/C) pilot manually controls the 'leader' throughout the flight. Each 'follower' executes the formation control laws to maintain a pre-defined position and orientation with respect to the 'leader'. A main objective of the controller design is to maintain the formation geometry under maneuvered flight conditions. In addition, a minimum amount of information exchange is also desired between the 'leader' and 'follower' aircraft.

Since the trajectory dynamics generally have a much larger time constant than the attitude dynamics, the formation controller can be designed with an inner/outer-loop structure. In this configuration, the outer-loop controller minimizes the lateral, forward, and vertical distance error while the inner-loop controller performs disturbance attenuation and attitude tracking. The definition of formation geometry and designs of the inner-loop and outer-loop controllers are described next.

2.1 Formation Geometry

Consider that the flight path typically lies in a horizontal plane, the formation flight control can be simplified as two decoupled horizontal and vertical tracking problems. The general

formation geometry is shown in Fig. 1. For navigation purposes, the position and velocity of both 'leader' and 'follower' aircraft are expressed with respect to a pre-defined Local Tangent Plane (LTP) and are measured by the on-board GPS receivers.

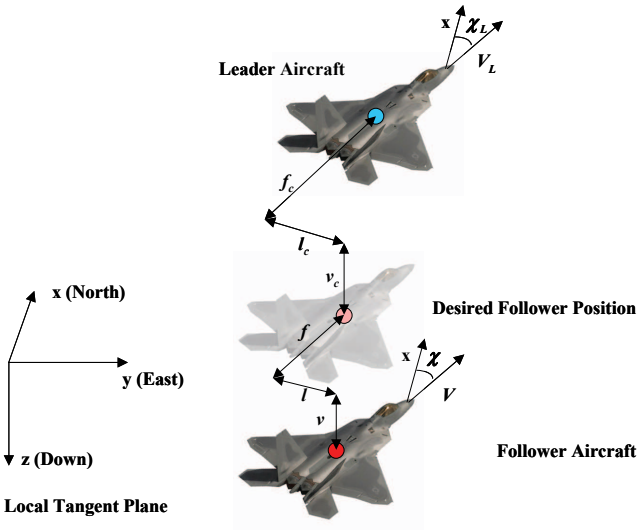

Figure 1. Formation Geometry

A. Horizontal Geometry

The horizontal formation geometric parameters include the desired forward clearance f_c and the desired lateral clearance l_c, as defined in Fig. 1. The forward distance error f and lateral distance error l can be calculated using the following relationship:

$$\begin{bmatrix} l \\ f \end{bmatrix} = \begin{bmatrix} \sin(\chi_L) & -\cos(\chi_L) \\ \cos(\chi_L) & \sin(\chi_L) \end{bmatrix} \begin{bmatrix} x_L - x \\ y_L - y \end{bmatrix} - \begin{bmatrix} l_c \\ f_c \end{bmatrix} \tag{1}$$

, where χ is the aircraft azimuth angle, x and y are the aircraft position along the x and y axis, and a subscript '$_L$' is used for all 'leader' parameters. A trigonometric expression for the azimuth angle is given as:

$$\sin(\chi) = \frac{V_y}{\sqrt{V_x^2 + V_y^2}} \tag{2}$$

, where V_x and V_y are the projections of the velocity along the x and y axes of the LTP. Equation (1) transforms the position error from an LTP reference frame to a reference frame oriented along the velocity of the 'leader'. In addition, the derivatives of f and l can be described as:

$$\begin{bmatrix} \dot{\ell} \\ \dot{f} \end{bmatrix} = \begin{bmatrix} V_{xy} \sin(\chi - \chi_L) \\ V_{Lxy} - V_{xy} \cos(\chi - \chi_L) \end{bmatrix} + \Omega_L \begin{bmatrix} f \\ -\ell \end{bmatrix} \tag{3}$$

, where Ω is the aircraft angular turn rate and V_{xy} is the aircraft velocity in the horizontal plane. It is obvious that the lateral and forward distance controls are coupled.

B. Vertical Geometry

The vertical distance error v can be obtained as:

$$v = z_L - z - v_c \tag{4}$$

, where v_c is the desired vertical clearance and z is the aircraft position along the z axis. The vertical geometry is also shown in Fig. 1.

2.2 Outer-Loop Controller

The outer-loop controller is designed separately for the decoupled vertical and horizontal formation geometries. The vertical controller is a simple linear altitude tracker providing the desired pitch angle θ_d to be followed by the inner-loop controller

$$\theta_d = K_v v + K_{vs}\dot{v} \tag{5}$$

, where K is the feedback gain to be selected later.

The outer-loop horizontal controller calculates the desired throttle position δ_T and the desired roll angle command ϕ_d for the inner-loop control laws to follow:

$$\begin{bmatrix} \delta_T \\ \phi_d \end{bmatrix} = f(\chi - \chi_L, \begin{bmatrix} f \\ l \end{bmatrix}) \tag{6}$$

, where *f()* is a nonlinear function to be determined next. The design of the horizontal controller is based on a Non-Linear Dynamic Inversion (NLDI) approach, which algebraically transforms the nonlinear system into a linear one (Isidori 1995) (Slotine & Li 1991) (Calise & Rysdyk 1998) so that standard linear control techniques can be applied. The use of nonlinear technique provides an effective way for controlling the aircraft under a wide range of maneuvering conditions.

In this specific problem, to minimize the forward and lateral distance errors *f* and *l,* the desired bank angle ϕ_d and throttle command δ_T are used as outer-loop control inputs. From equation (3), the second derivatives of *f* and *l* can be calculated as:

$$\begin{bmatrix} \ddot{\ell} \\ \ddot{f} \end{bmatrix} = \begin{bmatrix} \sin(\chi - \chi_L) \\ -\cos(\chi - \chi_L) \end{bmatrix} \dot{V}_{xy} + \begin{bmatrix} \cos(\chi - \chi_L) \\ \sin(\chi - \chi_L) \end{bmatrix} V_{xy}(\Omega - \Omega_L) + \begin{bmatrix} f \\ -\ell \end{bmatrix} \dot{\Omega}_L + \begin{bmatrix} \dot{f} \\ -\dot{\ell} \end{bmatrix} \Omega_L \tag{7}$$

To establish the relationship between this equation and control inputs $[\delta_T, \phi_d]$, let's first look at the aircraft forward translational acceleration equation (Stevens & Lewis 1992):

$$\begin{aligned} \dot{V} &= \frac{1}{m}(Y\sin\beta - D\cos\beta + T\cos\alpha\cos\beta) - g\sin\gamma \\ &= \left(\frac{\cos\alpha\cos\beta}{m}\right)T - \left(\frac{\bar{q}S(C_D\cos\beta - C_Y\sin\beta)}{m} + g\sin\gamma\right) \triangleq \omega_1 T - \omega_2 \end{aligned} \tag{8}$$

, where *D*, *Y*, and *T* are the drag, side force, and thrust,, respectively, *m* is the aircraft mass, *g* is the acceleration due to gravity, *a*, β, and γ are the angle of attack, angle of sideslip, and

flight path angle, respectively, with $\cos\gamma = V_{xy}/V$, $\bar{q}$ is the dynamic pressure, S is the wing area, and C_D and C_Y are the dimensionless drag and side force coefficients.

The projection of $\dot{V}$ onto the level plan is given by (assuming a quasi steady state condition with $\dot{\gamma} = 0$):

$$\dot{V}_{xy} = \dot{V}\cos\gamma = T\omega_1\cos\gamma - \omega_2\cos\gamma = \frac{V_{xy}}{V}\omega_1 T - \frac{V_{xy}}{V}\omega_2 = \frac{V_{xy}}{V}\omega_1(T_b + K_T\delta_T) - \frac{V_{xy}}{V}\omega_2 \tag{9}$$

, where T_b and K_T are constants to be provided by the aircraft propulsion model. Assuming a coordinated turn condition for both the 'leader' and 'follower' aircraft:

$$\Omega = \dot{\chi} \cong \dot{\psi} \cong \frac{g}{V}\tan\phi \tag{10}$$

, where ψ is the aircraft heading angle and ϕ is the roll angle. Also assuming a steady wings-level or steady turning flight condition for the 'leader':

$$\dot{\Omega}_L = 0 \tag{11}$$

equation (7) becomes

$$\begin{aligned}\begin{bmatrix}\ddot{\ell}\\ \ddot{f}\end{bmatrix} = &\begin{bmatrix} V_{xy}\cos(\chi-\chi_L) & \frac{V_{xy}}{V}\omega_1\sin(\chi-\chi_L)\\ V_{xy}\sin(\chi-\chi_L) & -\frac{V_{xy}}{V}\omega_1\cos(\chi-\chi_L)\end{bmatrix}\begin{bmatrix}\frac{g}{V}\tan(\phi_d)\\ T_b + K_T\delta_T\end{bmatrix} + \frac{V_{xy}}{V}\omega_2\begin{bmatrix}-\sin(\chi-\chi_L)\\ \cos(\chi-\chi_L)\end{bmatrix}\\ &-\Omega_L V_{xy}\begin{bmatrix}\cos(\chi-\chi_L)\\ \sin(\chi-\chi_L)\end{bmatrix} + \Omega_L\begin{bmatrix}\dot{f}\\ -\dot{\ell}\end{bmatrix}\end{aligned} \tag{12}$$

Since the (2 x 2) matrix relating inputs and second derivatives of the output from (12) is invertible, the resulting inversed relationship is given by:

$$\begin{aligned}\begin{bmatrix}\frac{g}{V}\tan(\phi_d)\\ T_b + K_T\delta_T\end{bmatrix} = &\frac{1}{V_{xy}}\begin{bmatrix}\cos(\chi-\chi_L) & \sin(\chi-\chi_L)\\ \frac{V}{\omega_1}\sin(\chi-\chi_L) & -\frac{V}{\omega_1}\cos(\chi-\chi_L)\end{bmatrix}\begin{bmatrix}\ddot{\ell}_d\\ \ddot{f}_d\end{bmatrix}\\ &+\begin{bmatrix}\Omega_L\\ \frac{\omega_2}{\omega_1}\end{bmatrix} + \begin{bmatrix}\dot{\ell}\sin(\chi-\chi_L) - \dot{f}\cos(\chi-\chi_L)\\ -\frac{V}{\omega_1}\dot{\ell}\cos(\chi-\chi_L) - \frac{V}{\omega_1}\dot{f}\sin(\chi-\chi_L)\end{bmatrix}\frac{\Omega_L}{V_{xy}}\end{aligned} \tag{13}$$

By imposing $\alpha = \alpha_0$, $\beta = 0$, the lateral NLDI control law is:

$$\begin{aligned}\phi_d = \arctan\Bigg\{&\frac{1}{g\cos\gamma}\left[\ddot{\ell}_d\cos(\chi-\chi_L) + \ddot{f}_d\sin(\chi-\chi_L)\right]\\ &+\frac{V}{g}\Omega_L + \left[\dot{\ell}\sin(\chi-\chi_L) - \dot{f}\cos(\chi-\chi_L)\right]\frac{\Omega_L}{g\cos\gamma}\Bigg\}\end{aligned} \tag{14}$$

and the forward control law is:

$$\begin{aligned}\delta_T = &\frac{m}{K_T \cos\gamma}\left[\ddot{\ell}_d \sin(\chi-\chi_L) - \ddot{f}_d \cos(\chi-\chi_L)\right] \\ &+\frac{1}{K_T}\left(\frac{1}{2}\rho_0 V^2 S\left(C_{D0}+C_{D\alpha}\alpha_0\right)+m\sin\gamma - T_b\right) \\ &-\frac{m}{K_T\cos\gamma}\Omega_L\left[\dot{\ell}\cos(\chi-\chi_L)+\dot{f}\sin(\chi-\chi_L)\right]\end{aligned} \tag{15}$$

The application of the control inputs (14) and (15) to the system described by (12) cancels the non-linearities, leading to the linear relationship:

$$\begin{bmatrix}\ddot{\ell}\\ \ddot{f}\end{bmatrix} = \begin{bmatrix}\ddot{\ell}_d\\ \ddot{f}_d\end{bmatrix} \tag{16}$$

, which can be controlled with compensator-type linear control laws:

$$\begin{aligned}\ddot{\ell}_d &= -K_{\ell s}\dot{\ell} - K_\ell \ell \\ \ddot{f}_d &= -K_{fs}\dot{f} - K_f f\end{aligned} \tag{17}$$

2.3 Inner-Loop Controller

The objective of the inner-loop controller design is to achieve desirable disturbance attenuation and tracking capabilities while maintaining a reasonable stability margin and damping ratio. The longitudinal inner-loop control law tracks the desired pitch angle, as supplied by the outer-loop controller, using the following relationship:

$$i_H = K_q q + K_\theta(\theta - \theta_d) \tag{18}$$

, where i_H is the aircraft stabilator deflection, q is the roll rate, and θ is the roll angle.

The lateral-directional inner-loop control laws track a desired bank angle, supplied by the outer-loop controller, while augmenting the lateral-directional stability of the aircraft:

$$\delta_A = K_p p + K_\phi(\phi - \phi_d) \tag{19}$$

$$\delta_R(s) = K_r \frac{s}{s+\omega_0} r \tag{20}$$

where δ_A and δ_R are the aileron and rudder deflections, p and r are the pitch and yaw rates, ϕ is the pitch angle, and ω_0 is the washout filter constant to be selected.

3. Test-Bed Development

3.1 Aircraft Platform

A set of three YF-22 research aircraft were designed and developed for the formation flight experiments. Although these aircraft feature similarities with the Lockheed's YF-22 aircraft, they are not dynamically scaled models. Instead, the research team focused on designing

aircraft that could provide desirable handling quality and payload capacity. The WVU YF-22 fleet is shown in Fig. 2. Additional information about the design and manufacturing of the WVU YF-22 research aircraft is available at (Napolitano 2005).

Figure 2. WVU YF-22 Research Aircraft (Formation Flight Fleet)

An overview of the aircraft specifications is provided in Table 1.

Wingspan	1.96 m
Length	3.05 m with probe
Height	0.61 m
Wing Area	1.37 m^2
Weight	23 Kg
Fuel Capability	3.5 L
Maximum Flight Duration	12 minutes
Cruise Airspeed	42 m/s
Takeoff Speed	30 m/s
Engine / Thrust	RAM1000 / 125 N
T/W Ratio (fully fueled)	0.55
W/S Ratio (fully fueled)	16.5 Kg/ m^2

Table 1. Specifications of the test-bed aircraft

During takeoff/landing and part of the flight, the aircraft is under manual control with a 10-channel Pulse Code Modulation (PCM) R/C system. The ground pilot has control of the aircraft primary control surfaces (stabilators, ailerons, and rudders), secondary control surfaces (flaps), engine throttle, brakes, and a 'controller switch' to activate/deactivate the on-board autonomous flight control.

The turbine propulsion system generates up to 125 N of thrust. An Electronic Control Unit (ECU) monitors the exhaust gas temperature and engine compressor pressure, and, in turn, controls the turbine RPM by regulating the fuel supplied to the turbine. The fuel consumption is rated at approximately 0.35 liter/minute for a maximum RPM (127,000) setting. Throughout the flight experiment, with exception of the takeoff phase, the throttle

setting is typically within the (½ - ¾) range, with fuel consumption in the range of (0.15-0.3) liter/minute.

3.2 Avionics System

The avionics system is designed as a modulated system to meet the requirements of a wide range of research topics including formation flight control, fault-tolerant flight control, and vision-based navigation. Each 'follower' aircraft equips a complete set of avionics capable of data acquisition, communication, and flight control. It receives the 'leader' position information at a 50Hz update rate through a 900 Hz RF modem. The 'leader' avionics is a stripped down version of the 'follower' avionics with main objectives as data acquisition and communication. Fig. 3 shows the formation configuration and capabilities of the 'leader' and 'follower' avionics systems.

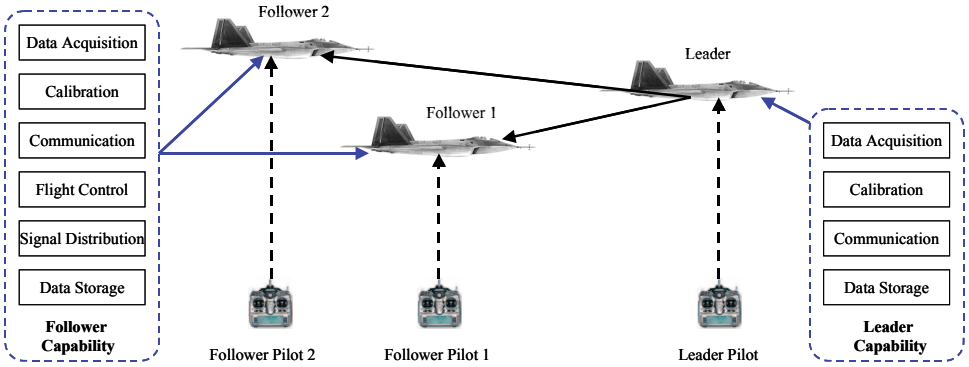

Figure 3. Formation Configuration and Capabilities

A view of the installed 'follower' avionics system is shown in Fig. 4. In general, the avionics receives pilot commands, monitors aircraft states, performs data communication, generates formation control commands, and distributes control signals to primary control surfaces and the propulsion system. A description of major avionics sub-systems is provided next.

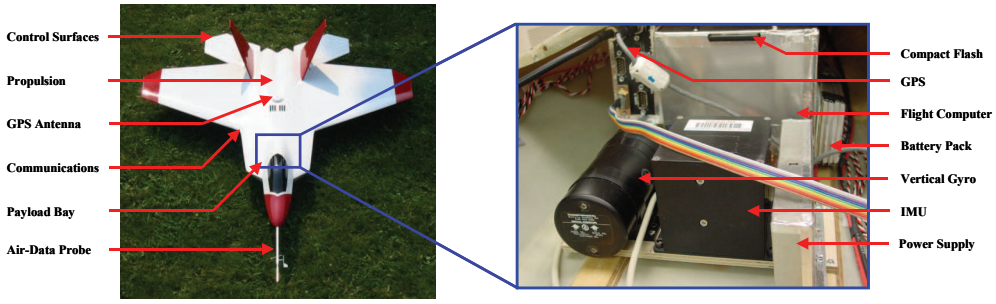

Figure 4. 'Follower' Aircraft and Avionics System

A. Flight Computer

The flight computer is based on a PC-104 format computer stack with a 300Mhz CPU module, a 32-channel 16-bit data acquisition module, a power supply/communication module, and an IDE compact flash adapter. In addition, a set of custom Printed Circuit

Board (PCB) was developed for interfacing sensor components, generating Pulse-Width Modulation (PWM) control signals, and distributing signals to each control actuator. The PC-104 format is selected because of its compact size and expandability. An 8 MB compact flash card stores the operation system, the flight control software, and the collected flight data. A 14.8v 3300mAh Li-Poly battery pack can power the avionics system for more than an hour, providing sufficient ground testing and flight mission time.

B. Sensor Suite

Flight data is collected and calibrated on-board for both real-time control and post-flight analysis. The sensor suite include a SpaceAge mini air-data probe, two SenSym pressure sensors, a Crossbow IMU400 Inertial Measurement Unit (IMU), a Goodrich VG34 vertical gyro, a Novatel OEM4 GPS receiver, a thermistor, and eight potentiometers measuring primary control surfaces deflections (stabilators, ailerons, rudders) and flow angles (α, β). A digital video camera is also installed on one of the 'followers' for flight documentation. A total of 22 analog channels are measured with a 16-bit resolution. The sampling rate was initially set at 100 Hz for data acquisition flights and later reduced to 50 Hz for matching the control command update rate (limited by the R/C system). Consider the aircraft short period mode of 7.7 rad/sec (1.2 Hz), a 50 Hz sampling rate provides a substantial amount of oversampling.

The analog signals measured on-board include absolute pressure (0-103.5 kPa), dynamic pressure (0-6.9 kPa), angle of attack (±25°), sideslip angle (±25°), air temperature (-10-70°C), roll angle (±90°), pitch angle (±60°), 3-axis accelerations (±10g), 3-axis angular rates (±200°/sec), 6-channel primary control surfaces deflections (±15°), and several avionics health indicators. A GPS receiver provides direct measurements of the aircraft 3-axis position and velocity with respect to an Earth-Centered-Earth-Fixed (ECEF) Cartesian coordinate system. These measurements are then transformed into a LTP used by the formation controller. The GPS measurement is updated at a rate of 20 Hz, providing a substantial advantage over the low-cost 1Hz GPS system.

C. Control Signal Distribution System

A Control Signal Distribution System (CSDS) is designed to give the 'follower' pilot the freedom to switch between manual and autonomous modes at any time during the flight. A block diagram for the CSDS is shown in Fig. 5.

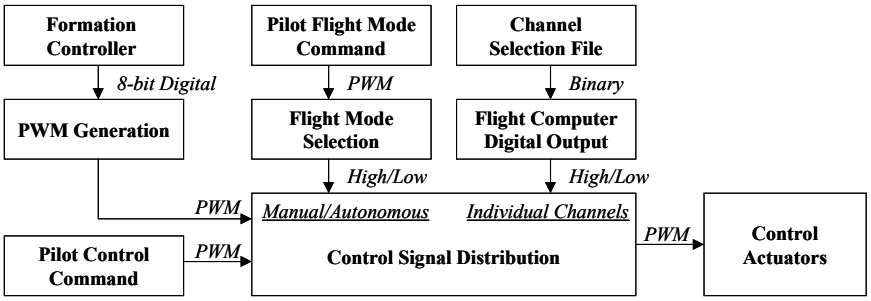

Figure 5. Control Signal Distribution System

During the autonomous mode, the flight computer can have control of all or a subset of six control channels including the left stabilator, right stabilator, left aileron, right aileron, dual rudders, and engine throttle. Two switching mechanisms are designed to ensure the safety of the aircraft - 'Hardware Switching' and 'Software Switching'. 'Hardware Switching'

allows the pilot to switch back to manual control instantly under any circumstance. In the case of avionics power loss, the manual control is engaged automatically. 'Software Switching' gives the flight computer the flexibility of controlling any combination of the aircraft's primary control surfaces and propulsion with pre-programmed selections. The 'Software Switching' is implemented through a synthesis of both hardware and software modules. Specifically, the on-board software reads pre-determined channel selection information from a log file during the initialization stage of the execution. Once the 'controller switch' is activated, the software sends out the channel selection signal through the digital output port of the data acquisition card. This signal is then passed to a controller board to select the pilot/on-board control. By using this feature, individual components of the flight control system can be tested independently. This, in turn, increases the flexibility and improves the safety of the flight-testing operation.

F. Electro-Magnetic Interference

Electro-Magnetic Interference (EMI) can pose significant threats to the safety of the aircraft. This is especially true for small UAVs, where a variety of electronic components are confined within a limited space. The most vulnerable part of the avionics system is often the R/C link between the ground pilot and the aircraft, which directly affects the safety of the aircraft and ground crew. Being close in distance to several interference sources such as the CPU, vertical gyro, RF modem, and any connection cable acting as an antenna, the range of the R/C system can be severely reduced. Since prevention is known to be the best strategy against EMI, special care is incorporated into the selection of the 'commercial-off-the-shelf' products as well as the design and installation of the customized components. Specifically, low pass filters are designed for the power system; all power and signal cables are shielded and properly grounded; and aluminum enclosures are developed and sealed with copper or aluminum tape to shield the hardware components. Once the avionics system is integrated within the airframe, ferrite chokes are installed along selected cables based on the noise level measured with a spectrum analyzer. Nevertheless, although detailed lab EMI testing has been proven important, because of the unpredictable nature of the EMI issue, strict R/C ground range test procedures are followed before each takeoff to ensure the safety of the flight operation.

4. Modeling and Parameter Identification

The availability of an accurate mathematical model of the test-bed is critical for the selection of formation control parameters and the development of a high-fidelity simulation environment. The modeling process is mainly based on the empirical data collected through both ground tests and flight-testing experiments.

4.1 Identification of the Aircraft Linear Mathematical Model

The decoupled linear aircraft model is determined through a Parameter IDentification (PID) effort. A series of initial test flights are performed to collect data used for the identification process. Typical pilot-injected maneuvers, including stabilator doublets, aileron doublets, rudder doublets, and aileron/rudder doublets, are performed with various magnitudes to excite the aircraft longitudinal and lateral-directional dynamics. Fig. 7 represents a typical aileron/rudder doublets maneuver, where a rudder doublet is performed immediately after an aileron doublet.

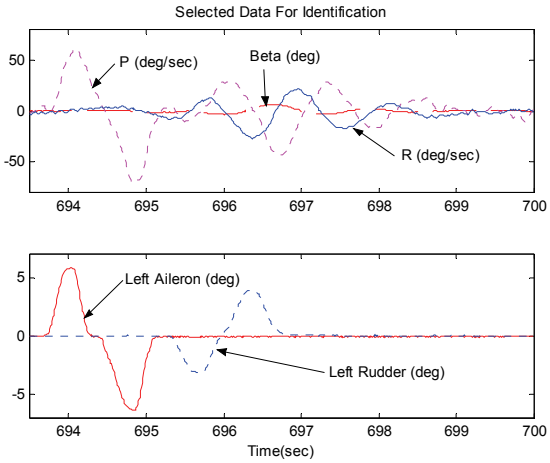

Figure 6. Flight Data for Linear Model Identification

The identification of the linear model is performed using a 3-step process. First, after a detailed examination of the flight data, two data segments with the best quality for each class of maneuvers are selected. Next, a subspace-based identification method (Ljung 1999) is used to perform the parameter identification with one set of data. Finally, the identified linear model is validated through comparing the simulated aircraft response with the remaining unused data set. This identification process is repeated until a satisfactory agreement is achieved. Following the identification study, the estimated linear longitudinal and lateral-directional aerodynamic model in continuous time are found to be:

$$\begin{bmatrix} \dot{V}_T \\ \dot{\alpha} \\ \dot{q} \\ \dot{\theta} \end{bmatrix} = \begin{bmatrix} -0.284 & -23.096 & 0 & -0.171 \\ 0 & -4.117 & 0.778 & 0 \\ 0 & -33.884 & -3.573 & 0 \\ 0 & 0 & 1 & 0 \end{bmatrix} \begin{bmatrix} V_T \\ \alpha \\ q \\ \theta \end{bmatrix} + \begin{bmatrix} 20.168 \\ 0.544 \\ -39.085 \\ 0 \end{bmatrix} i_H \tag{21}$$

$$\begin{bmatrix} \dot{\beta} \\ \dot{p} \\ \dot{r} \\ \dot{\phi} \end{bmatrix} = \begin{bmatrix} 0.430 & 0.094 & -1.030 & 0.237 \\ -67.334 & -7.949 & 5.640 & 0 \\ 20.533 & -0.655 & -1.996 & 0 \\ 0 & 1 & 0 & 0 \end{bmatrix} \begin{bmatrix} \beta \\ p \\ r \\ \phi \end{bmatrix} + \begin{bmatrix} 0.272 & -0.771 \\ -101.845 & 33.474 \\ -6.261 & -24.363 \\ 0 & 0 \end{bmatrix} \begin{bmatrix} \delta_A \\ \delta_R \end{bmatrix} \tag{22}$$

, where V_T is the true airspeed. This model represents the aircraft in a steady and level flight at V_T= 42 m/s, H= 310 m above the sea level, at trimmed condition with α = 3 deg, with inputs i_H = -1°, δ_A = δ_R =0° and a thrust force along the x body axis of the aircraft T = 54.62 N. The decoupled linear model is used later for the formation controller design.

4.2 Identification of the Non-Linear Mathematical Model

A more detailed non-linear mathematical model is identified for the development of a formation flight simulator. The identification process for a non-linear dynamic system relies

on detailed knowledge of the system dynamics along with the application of minimization algorithms (Maine & Iliff 1986). In general, the non-linear model of an aircraft system can be described using the following general form (Stevens & Lewis 1992), (Roskam 1995):

$$\begin{aligned} \dot{x} &= f(x,\delta,G,F_A(x,\delta),M_A(x,\delta)); \\ y &= g(x,\delta,G,F_A(x,\delta),M_A(x,\delta)); \end{aligned} \tag{23}$$

where x is the state vector, y is the output vector, δ is the input vector, G is a vector of geometric parameters and inertia coefficients, and F_A and M_A are aerodynamic forces and moments acting on the aircraft. The functions f and g are known as analytic functions modeling the dynamics of a rigid-body system. The aerodynamic forces and moments are expressed using the aerodynamic coefficients (Roskam 1995), including drag coefficient C_D, side force coefficient C_Y, lift coefficient C_L, rolling moment coefficient C_l, pitching moment coefficient C_m, and yawing moment coefficient C_n:

$$F_A = \bar{q}S\begin{bmatrix} C_D(x,\delta) \\ C_Y(x,\delta) \\ C_L(x,\delta) \end{bmatrix}, \quad M_A = \bar{q}S\begin{bmatrix} bC_l(x,\delta) \\ \bar{c}C_m(x,\delta) \\ bC_n(x,\delta) \end{bmatrix} \tag{24}$$

The moments of inertia of the aircraft are experimentally evaluated with a 'swing pendulum' experimental set-up (Soule & Miller 1934), as shown in Fig. 7

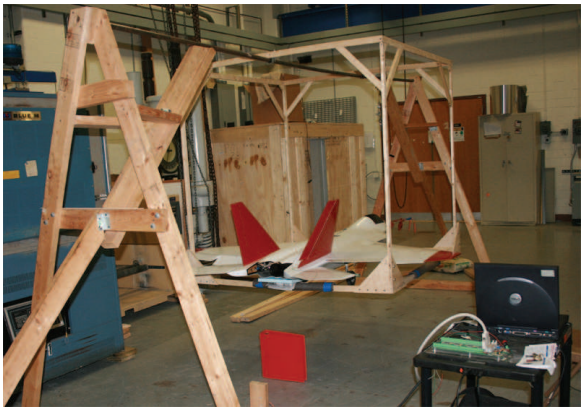

Figure 7 Experimental Setup for Measuring Aircraft Moments of Inertia

The product of inertia *Ixz* could not be evaluated using the pendulum-based method. Thus, the remaining issue is to determine *Ixz* along with the values of the aerodynamic derivatives of the aircraft. The relationship from the coefficients of the linear models (21) and (22) to the values of the aerodynamic derivatives and geometric-inertial parameters are known (Stevens & Lewis 1992). After inverting these relationships and using the experimental values of the geometric and inertial parameters, initial values for each of the aerodynamic stability derivatives are calculated. A Sequential Quadratic Programming (SQP) technique (Hock & Schittowski 1983) is then used to iteratively minimize the Root Mean Square (RMS) of the difference between the actual and simulated aircraft outputs [Campa et al. 2007]. The resulting non-linear mathematical model is given by:

Geometric and inertial:

$\bar{c}$ = 0.76 m, b = 1.96 m, S = 1.37 m²
I_{xx} = 1.61 Kg m², I_{yy} = 7.51 Kg m², I_{zz} = 7.18 Kg m², I_{xz} = -0.24 Kg m²
M = 20.64 Kg, T = 54.62 N

Longitudinal aerodynamic derivatives:

C_{D0} = 0.0085, C_{Da} = 0.5079, C_{Dq} = 0.0000, C_{DiH} = -0.0339
C_{L0} = -0.0492, C_{La} = 3.2580, C_{Lq} = -0.0006, C_{LiH} = 0.1898
C_{m0} = 0.0226, C_{ma} = -0.4739, C_{mq} = -3.4490, C_{miH} = -0.3644

Lateral-Directional aerodynamic derivatives:

C_{Y0} = 0.0156, $C_{Y\beta}$ = 0.2725, C_{Yp} = 1.2151,
C_{Yr} = -1.1618, $C_{Y\delta A}$ = 0.1836, $C_{Y\delta R}$ = -0.4592
C_{l0} = -0.0011, $C_{l\beta}$ = -0.0380, C_{lp} = -0.2134,
C_{lr} = 0.1147, $C_{l\delta A}$ = -0.0559, $C_{l\delta R}$ = 0.0141
C_{n0} = -0.0006, $C_{n\beta}$ = 0.0361, C_{np} = -0.1513,
C_{nr} = -0.1958, $C_{n\delta A}$ = -0.0358, $C_{n\delta R}$ = -0.0555

where $\bar{c}$ is the mean aerodynamic chord, b is the wing span, S is the wing area, and m is the aircraft mass with a 60% fuel capacity.

A final validation of the non-linear model is then conducted using the validation flight data set, as it was performed for the linear mathematical model. Figure 8 shows a substantial agreement between the measured and the simulated data with the non-linear model.

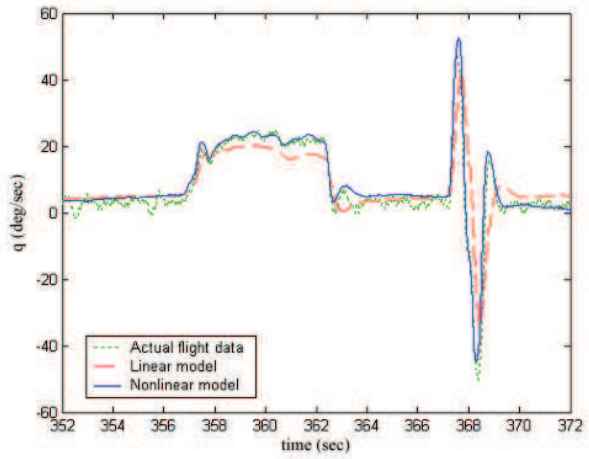

Figure 8. Linear and Non-linear Model Simulations Compared to Actual Flight Data

4.3 Engine and Actuator Models

The engine mathematical model is defined as the transfer function from the throttle command to the actual engine thrust output. The evaluation of this model is important as the jet propulsion system has a substantially lower bandwidth compared with rest of the control system. Fig. 9 provides a photo and a schematic drawing of the experimental set-up used for the identification process.

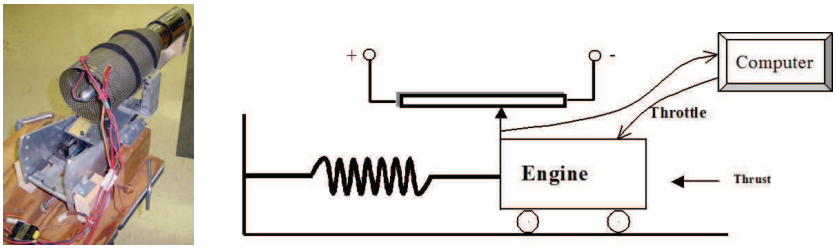

Figure 9. Engine Ground Test Setup and Schematic

The turbine is mounted on a customized engine test stand where the motion is limited to be only along the thrust force (x) direction. The thrust is then measured by reading the displacement of a linear potentiometer. The throttle control is based on 8-bit PWM signal generated by the computer with a throttle range between 0 and 255. During the test, a sequence of throttle commands is sent to the turbine and the corresponding thrust is measured with the data acquisition system, as shown in Fig. 10.

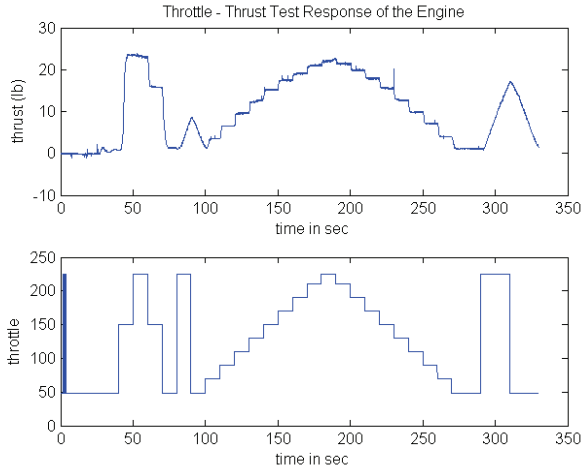

Figure 10. Throttle Thrust Response in Test Time Sequence

The first step of the engine model identification is to identify the static gain of the engine response from the throttle position to the thrust output. For simplicity purposes, a linear fitting is used. The linearized input-output relationship under steady-state condition is found to be:

$$T(N) = T_b + K_T \delta_T \tag{25}$$

, with $K_T = 0.624$ and $T_b = -25.86$.

To quantify the transient response of the engine dynamics, a standard prediction error method is applied to selected data segments where the throttle input consists of a series of step-like signals, as shown in Fig. 10. The identification result shows that the engine dynamic response can be approximated with a 1st order system and a pure time delay:

$$G_T(s) = \frac{T(s) - T_b}{\delta_T(s)} = \frac{K_T}{1 + \tau_T s} e^{-\tau_d s} \tag{26}$$

, with $\tau_T = 0.25\text{sec}$, and $\tau_d = 0.26\text{sec}$. As indicated by the values of τ_T and τ_d , the low bandwidth of the turbine propulsion system poses a fundamental limitation of the achievable formation flight performance under maneuvered flight conditions.

Digital R/C servos are used as actuators for the aircraft primary control surfaces. The actuator dynamics is defined as the transfer function from the 8-bit digital command to the actuator's actual position. During ground experiments, a set of step inputs is sent to the actuator. Both the control command and aircraft surface deflection are then recorded. The procedure is repeated for all six actuators on each of the primary control surfaces. From data analysis it is found that the actuator model could be approximated by the following transfer function:

$$G_{Act}(s) = \frac{1}{1 + \tau_a s} e^{-\tau_{ad} s} \tag{27}$$

where the actuator time constant τ_a and the time delay constant τ_{ad} were identified to be 0.04 sec and 0.02 sec respectively.

5. Controller Implementations and Simulation

5.1 Controller Parameters

Once a complete set of aircraft mathematical model is available, controller parameters are designed based on the classic root-locus method. The time delays in the engine model (26) and actuator model (27) are replaced by 1st order Pade approximations to facilitate the controller design. The final selections of controller parameters are listed in Table 2.

Inner-Loop Controller			Outer-Loop Controller		
Longitudinal	Lateral	Directional	Forward	Lateral	Vertical
$K_q = 0.12$	$K_p = 0.04$	$K_r = 0.16$	$K_f = 0.24$	$K_\ell = 0.20$	$K_v = 3.23$
$K_\theta = 0.50$	$K_\phi = 0.35$	$\omega_0 = 1.80$	$K_{fs} = 2.06$	$K_{\ell s} = 0.89$	$K_{vs} = 1.76$

Table 2. Formation Controller Parameters

5.2 Simulation Environment

A Simulink®-based formation flight simulation environment is developed using the mathematical model and the formation control laws described in previous sections. This environment provides a platform for validating and refining the formation control laws prior to performing the actual flight tests. The simulation schemes are interfaced with the Matlab® Virtual Reality Toolbox (VRT), where objects and events of a virtual world can be driven by signals from the simulation. The collected flight data can also be played back 'side-by-side' with the simulated aircraft response. This provides an important tool for validating the accuracy of the identified nonlinear aircraft model. In addition, the ability for VRT to visualize the entire formation flight operation, especially with the freedom of selecting different viewpoints, provides a substantial amount of intuition during the

controller design and flight planning process. Figure 11 shows the formation flight simulation environment.

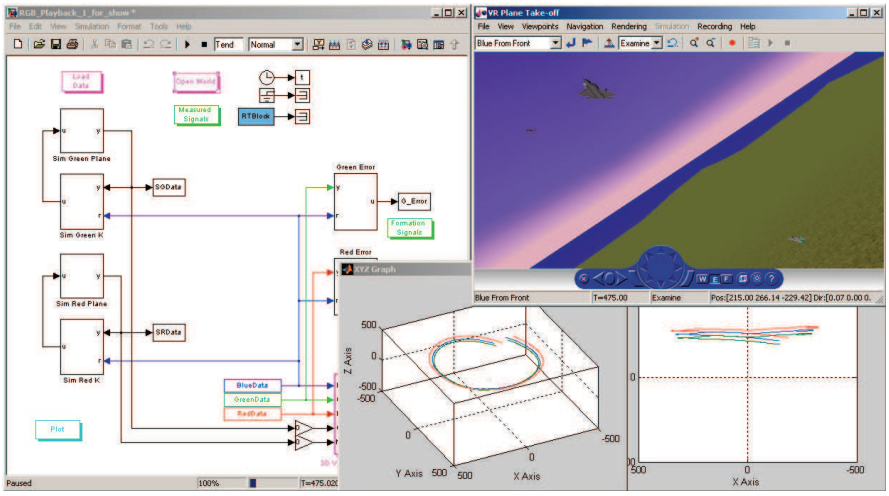

Figure 11. Formation Flight Simulation Environment

5.3 Robustness Assessment

The robustness of the formation controller is investigated with a Monte Carlo method, where a series of simulation studies is performed to evaluate the degradation of the close-loop stability and tracking performance caused by the measurement noise and modeling error. The following two formation configurations are analyzed:

$$\text{Configuration \#1:} \qquad l_c = -20m, \quad f_c = 20m, \quad v_c = 20m \tag{28}$$

$$\text{Configuration \#2:} \qquad l_c = 20m, \quad f_c = 20m, \quad v_c = -20m \tag{29}$$

These two configurations are later used during the flight-testing program. To simulate the effects of the measurement error/noise, a set of random noise is applied on all inputs of the formation controller. Specifically, random values following Gaussian distributions with zero means are added to the simulation parameters using the following standard deviation values:

- 2 deg/sec for angular rates (p, q, r);
- 2 deg for Euler angles (θ, ϕ);
- 4 m for horizontal position components (x,y);
- 8 m for vertical position component (z);
- 2 m/sec for horizontal velocity components (V_x, Vy);
- 4 m/s for vertical velocity component (V_z).

These values are substantially higher than the typical measurement noise observed in the actual flight data. Simulation studies reveal that the average tracking error increased by 6% and 20% for configurations #1 and #2, respectively, compared to the ideal conditions without measurement error.

An assessment of the closed-loop stability with the existence of multiplicative modeling uncertainties is also performed with a 2-step process. First, a ±10% variation is applied on each of the 30 longitudinal and lateral-directional aerodynamic derivatives, one at a time. Simulation studies show no unstable conditions for all configurations with the three most sensitive coefficients found to be C_{Da}, C_{La}, and C_{ma}. The second step is to vary the value of these three coefficients along with seven additional parameters by ±5% and perform a simulation for each possible combination. The selected parameters are C_{D0}, C_{miH} , C_{Y0}, $C_{l\beta}$, C_{lp}, $C_{l\delta A}$, $C_{n\beta}$, $C_{n\delta R}$. Therefore, a batch set of simulations (2048 total) by varying combinations of parameter changes are performed using both formation configuration #1 and #2. Again, no unstable conditions are observed in this analysis. The worst-case degradation of tracking performance is found to be 1.98 m for the lateral distance error, 1.05 m for the forward distance error, and 4.41 m for the vertical distance error. Overall, the simulation result indicates that the designed formation controller has adequate robustness characteristics with respect to modeling errors.

5.4 On-Board Software

The formation controller software module, once validated through simulation studies, is integrated with other software components to perform real-time data acquisition, communication, and control. The on-board software is implemented as a Simulink scheme with each component written in C-language as a Matlab 'S-function'. An executable file is compiled using Matlab Real-Time Workshop (RTW) as a real-time extended DOS target for flight test experiments. The modulated software design provides flexibility for quick on-site reconfigurations to meet various flight-testing objectives.

The main tasks for 'leader' on-board software is to perform data acquisition, communication, and data storage. The 'follower' software also executes the formation control laws, selects the operational mode of the aircraft, decides primary control channels to be controlled on-board, and calibrates the flight control commands. Figure 12 shows a sample of the 'follower' on-board software scheme.

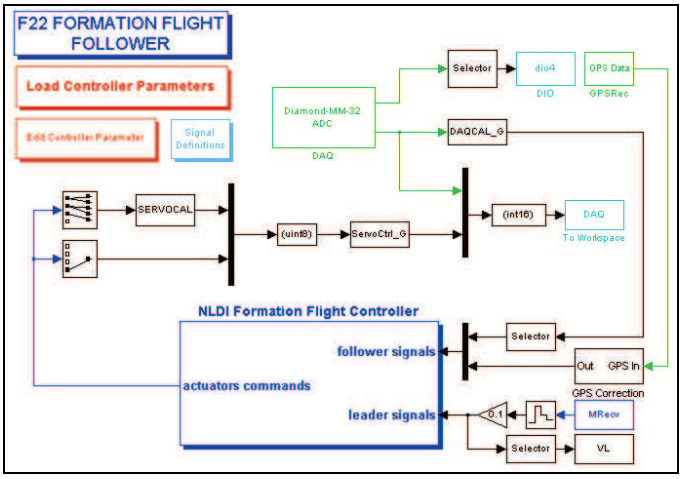

Figure12. Simulink Diagram of the 'Follower' Aircraft Software

6. Flight-Testing Of Formation Control Laws

Flight-testing is the most realistic step for controller validating and by far the most risky one. Despite the fact that the use of UAV can greatly reduce the risk associated with control system validation, careful planning is still of paramount importance for ensuring the safe operation and help identifying potential problems. This section provides an overview of different flight-testing phases and the outcomes of the autonomous formation flight experiments.

6.1 Flight Testing Phases

The flight-testing program is divided into six major phases with increasing complexity and risk level:

A. Flight for Assessment of Handling Qualities

This initial phase is for evaluating the handling qualities and dynamic characteristics of the test-bed aircraft. After a few satisfactory test flights, 'artificial' payloads of incremental weight are installed to test the structural integrity and the handling qualities under a full payload configuration.

B. Data Acquisition Flights

The avionics system is installed and flight data is collected for the PID analysis. A set of dedicated PID maneuvers is performed throughout multiple flights to excite the aircraft dynamics. Typical PID maneuvers include stablator doublets, aileron-rudder doublets, and a range of engine throttle inputs.

C. Inner-Loop Controller Validation

The stability and tracking performance of the designed inner-loop linear controller is validated during this phase. Both the longitudinal and lateral-directional inner-loop control laws are tested. The flight control hardware is also validated during this phase.

D. Outer-Loop Controller Sub-System Validation

Individual sub-systems of the outer-loop controller are tested. Experiments are performed to test the altitude-hold, heading-hold, and velocity-hold control and their combinations. Sample flight data in Fig. 13 shows the result from a heading-hold control experiment.

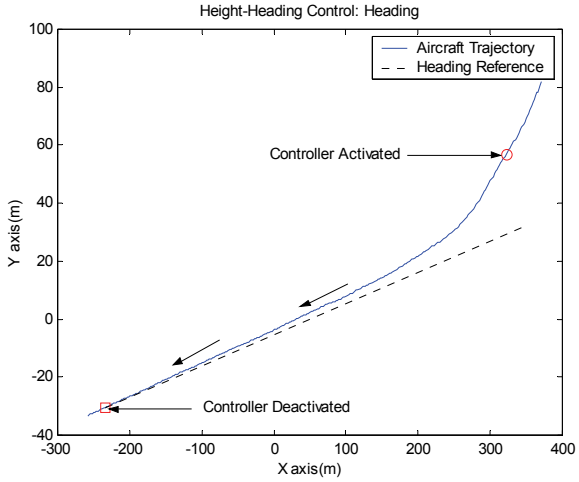

Figure 13. Heading Control Experiment

E. 'Virtual Leader' Flights

A 'Virtual Leader' (VL) approach is implemented as an alternative method for testing the formation controller without the risk and logistic issues associated with a full-blown multiple-aircraft experiment. The VL experiment consists of a single aircraft tracking a previously recorded flight trajectory. This trajectory is initially stored on-board the 'follower' aircraft and later moved to a ground station to test the performance of the communication link. The VL flights are proven to be invaluable for the validation and fine-tuning of formation control laws. A total of 12 VL flights are performed using various formation parameters. Fig. 14 is a sample flight data demonstrating the ability for the formation controller to reduce a large initial error and maintain the formation flight.

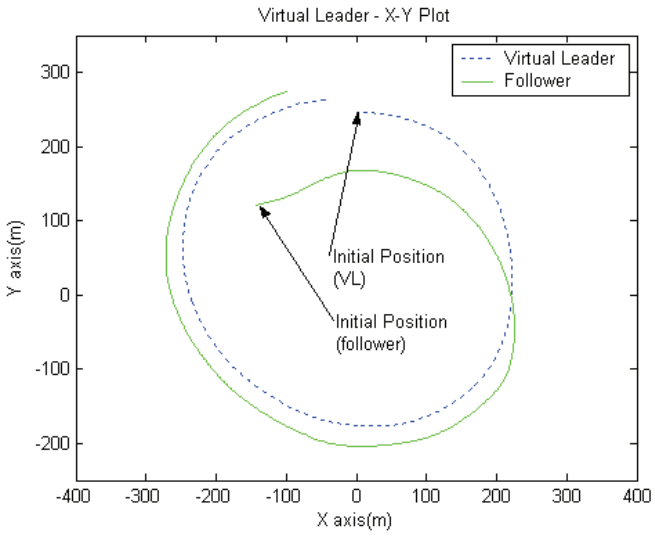

Figure 14. 'Virtual leader' Test - X-Y Plane

F. Multiple Aircraft Formation Flights

After various formation geometries and initial conditions are explored with the VL experiments, the flight-testing program proceeds to the multiple aircraft testing. A total of four 2-aircraft formation flight experiments are performed along with one 3-aircraft formation demonstration.

6.2 Three-Aircraft Formation Flight Experiment

The procedure for the 3-aircraft formation experiment is the following. The 'blue' aircraft, acting as the 'leader', takes off first while the 'red' aircraft ('follower #1') takes off approximately 35 seconds later. After the 'red' aircraft reaches a pre-defined 'rendezvous' area behind the 'leader', the ground pilot engages the on-board formation control. Once the 2-aircraft formation is stabilized for approximately 50 seconds, the 'green' aircraft ('follower #2') takes off and approaches a 'rendezvous' area behind the 2-aircraft already in formation. After the 'green' pilot engages the autonomous control, the trajectory of the 3-aircraft formation is solely controlled by the 'leader' R/C pilot. Fig. 15 shows a ground photo of the 3-aircraft formation experiment.

Figure 15. 3-Aircraft Formation Flight Test

The pre-selected formation geometries include configuration #1 (Equation 28) for the 'red' aircraft and configuration #2 (Equation 29) for the 'green' aircraft. Fig. 16 represents a 40-second portion of flight trajectory during the formation flight. The 3-aircraft formation configuration is engaged for approximately 275 seconds. Fig. 17 shows the aircraft altitude during the formation flight.

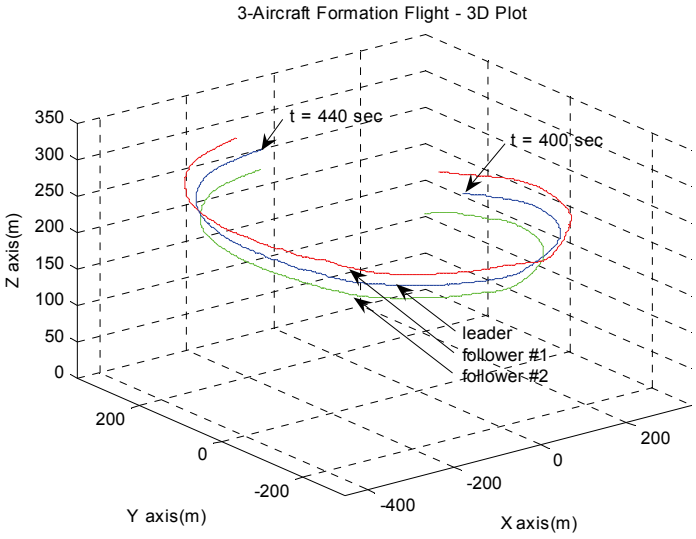

Figure 16. 3- Aircraft Formation Test - 3D Trajectory
(Blue='leader', Red=Outside 'follower', Green=Inside 'follower')

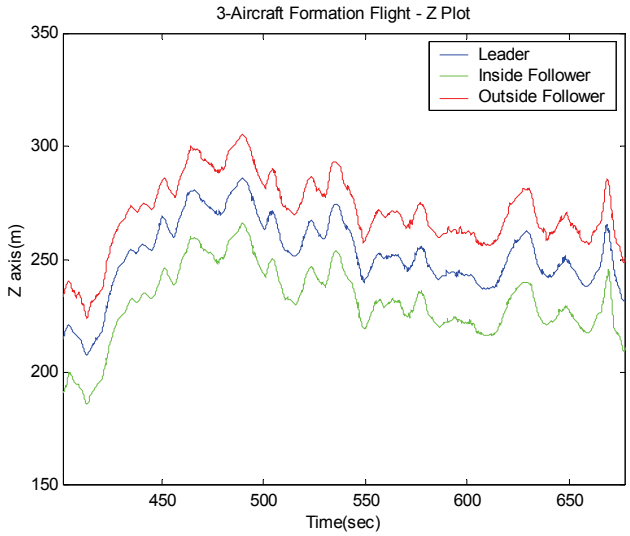

Figure 17. 3-Aircraft Formation Test - Altitude

The mean and standard deviation of the steady state tracking error for the flight test are shown in Table 3. The simulation results calculated with the same 'leader' trajectory are also supplied for comparison purposes.

3-aircraft formation Experiment		f_c (m)	l_c (m)	v_c (m)	Forward Distance Error (m)		Lateral Distance Error (m)		Vertical Distance Error (m)	
					Mean	Std. Dev	Mean	Std. Dev	Mean	Std. Dev
Green Aircraft	Flight Data	20	-20	20	-2.49	2.46	13.24	3.45	1.15	1.04
	Simulation	20	-20	20	-3.59	2.50	14.31	3.30	1.34	0.71
Red Aircraft	Flight Data	20	20	-20	27.28	3.73	-2.59	2.29	1.15	0.95
	Simulation	20	20	-20	25.30	3.82	-0.46	1.98	1.19	0.66

Table 3. 3-Aircraft Formation Test – Error Analysis

The 3-aircraft formation experiment validates the overall design of the formation controller, test-bed aircraft, and on-board avionics system. The statistical analysis shows that the 'outside' aircraft - 'follower #2' - achieves desirable lateral tracking performance but with a larger forward tracking error. On the contrary, the 'inside' aircraft shows desirable forward tracking and a slightly degraded lateral tracking performance. Both 'follower' aircraft exhibits excellent tracking performance for the vertical channel. Overall, the standard deviation for all of the tracking errors are found to be relatively small, with a maximum value of 3.73 m, showing a smooth trajectory following performance. In addition, a substantial agreement between the simulation result and actual flight data is noticed, indicating an accurate nonlinear mathematical model of the aircraft.

7. Conclusion

This chapter summarizes the results of an effort towards demonstrating closed-loop formation flight using research UAVs. A 'leader-follower' strategy is followed during the formation controller design. A two-time-scale approach is used with a nonlinear outer-loop and linear inner-loop controller. The flight-testing program was conducted over three flight seasons (2002 through 2004) with approximately 100 flight sessions. The incremental flight-testing phases validates the overall design of the formation control laws and the performance of the test-bed aircraft and avionics systems. The application of a 'virtual leader' technique proves to be an invaluable and safe approach for an initial testing of the formation control laws. During the final flight sessions, a total of five formation flight experiments are successfully performed, including four 2-aircraft formations and one 3-aircraft formation. Flight data confirms satisfactory performance for the designed 'leader-follower' type formation control laws.

8. References

Weimerskirch, H.; Martin, J.; Clerquin, Y.; Alexandre, P. & Jiraskova, S. (2001). Energy savings in flight formation. *Nature.* Vol. 413, pp. 697-698.

Scharf, D. P.; Hadaegh, F. Y. & Ploen, S. R. (2004). A survey of spacecraft formation flying guidance and control (part II): control. *American Control Conference*, Boston, MA, June 2004, pp. 2976–2985.

Dargan, J.L.; Patcher, M. & D'Azzo, J.J. (1992). Automatic formation flight control. *Proc. AIAA Guidance, Navigation and Control Conf.*. Hilton Head, SC, Aug. 1992, pp. 838-857.

Buzogany, L.E.; Patcher, M. & D'Azzo, J.J. (1993). Automated control of aircraft in formation flight. *Proc. AIAA Guidance, Navigation and Control Conf.*. Monterey, CA, Aug. 1993, pp. 1349-1370.

Veth, M.; Pachter, M. & D'Azzo, J.J. (1995). Energy preserving formation flight control. AIAA-1995-335, *Aerospace Sciences Meeting and Exhibit*, 33rd, Reno, NV, Jan 9-12, 1995

Reyna, V.P.; Pachter, M. & D'Azzo, J.J. (1994). Formation Flight. Control Automation. *Proc. AIAA Guidance, Navigation, and Control Conference,* pp 1379-1404,

McCammish, S.; Pachter, M.; D'Azzo, J. J. & Reyna, V. (1996) Optimal Formation Flight Control. *AIAA Guidance, Navigation, and Control Conference*, San Diego, CA, Jul. 1996.

Dogan, A.; Sato, S.; & Blake W. (2005). Flight Control and Simulation for Aerial Refueling. AIAA paper 2005-6264, *Proc. AIAA Guidance, Navigation, and Control Conference*, San Francisco, CA, Aug 15-18, 2005

Boskovic, J.D. & Mehra, R.K. (2003). An adaptive reconfigurable formation flight control design, *Proc. American Control Conference*. June 2003 Vol 1, pp. 284-289

Li, Y.; Li, B.; Sun, Z. & Song, Y.D. (2005). Fuzzy technique based close formation flight control. *Industrial Electronics Society*, 2005. IECON 2005. *32nd Annual Conference of IEEE*, Nov. 2005

Li, B.; Liao, X.H.; Sun, Z.; Li, Y.H. & Song, Y.D. (2006). Robust Autopilot for Close Formation Flight of Multi-UAVs, System Theory. *Proceeding of the Thrity-Eighth Southeastern Symposium*, March 2006, pp. 258- 262

Singh, S.N.; Chandler, P.; Schumacher, C.; Banda, S. & Pachter M. (2000). Adaptive feedback linearizing nonlinear close formation control of UAVs, *Proc. American Control Conference*, 2000. vol.2, pp.854-858

Venkataramanan, S. & Dogan, A. (2003). Nonlinear Control for Reconfiguration of UAV Formation. AIAA paper 2003-5725, *Proc. AIAA Guidance, Navigation, and Control Conference*, Austin, TX, Aug. 2003

Schumacher, C.J. & Singh, S.N. (2000). Nonlinear Control of Multiple UAVs in Close-Coupled Formation Flight. *AIAA Paper* 2000-4373, Aug. 2000

Allen, M.J.; Ryan, J.; Hanson, C.E. & Parle, J.F. (2002). String Stability of a Linear Formation Flight Control System. *AIAA Paper* 2002-4756, Aug. 2002

Giulietti, F.; Pollini, L. & Innocenti, M. (2000). Autonomous formation flight. *IEEE Control Systems Magazine*, Vol. 20, No. 6, pp. 34-44, Dec. 2000

Gingras, R.D. (1999). Experimental Investigation of a Multi-Aircraft Formation, *AIAA. Paper*-99-3143, 1999

Fowler, J. M. & D'Andrea, R. (2003). A formation flight experiment: Constructing a test-bed for research in control of interconnected systems. *Control Systems Magazine*, 23(5) pp.35-43, 2003

Kutay, A.T.; Fowler, J.M.; Calise, A.J. & D'Andrea, R. (2005). Distributed Adaptive Output Feedback Control Design and Application to a Formation Flight Experiment. *AIAA Guidance, Navigation and Control Conference*, August 2005

Napolitano, M.R. (2005). Development of formation flight control algorithms using 3 YF-22 flying models. *AFOSR Report* A994434, Apr. 2005, Available: (http://www.stormingmedia.us/99/9944/A994434.html)

Gu, Y.; Seanor, B.; Campa, G.; Napolitano, M.R.; Rowe, L.; Gururajan, S.; Perhinschi, M.G. & Wan, S. (2006). Design and Flight Testing Evaluation of Formation Control Laws. *IEEE Transactions on Control Systems Technology*, November 2006

Lavretsky, E. (2002). F/A-18 autonomous formation flight control system design. AIAA Guidance, Navigation and Control Conference, *AIAA Paper* 2002-4757, Monterey, CA, Aug. 2002.

Hanson, C.E.; Ryan, J.; Allen, M.J. & Jacobson, S.R. (2002). An Overview of Flight Test Results for a Formation Flight Autopilot. *AIAA Paper* 2002-4755, Aug. 2002

How, J. P.; King, E. & Kuwata, Y. (2004). Flight Demonstrations of Cooperative Control for UAV Teams. *Proc. AIAA 3rd Unmanned Unlimited Technical Conference, Workshop and Exhibit*, Sept. 2004. AIAA-2004-6490

Johnson, E.N.; Calise, A.J.; Sattigeri, R. & Watanabe, Y. (2004) Approaches to Vision-Based Formation Control. *Proc. IEEE Conference on Decision and Control*, December 2004.

Isidori, A. (1995). *Nonlinear Control Systems*, Springer-Verlag, London, Third edition, 1995.

Slotine, J.-J. E. & Li, W. (1991). Applied Nonlinear Control, Prentice Hall, New Jersey, 1991.

Calise, A.J. & Rysdyk, R.T. (1998). Nonlinear adaptive flight control using neural networks. *IEEE Control Systems Magazine*, Vol. 18, No. 6, pp. 14-25, Dec. 1998

Stevens, B. & Lewis, F. (1992). *Aircraft Control and Simulation*, John Wiley & Sons, NY, 1992.

Ljung, L. (1999). *System Identification: Theory for the User*, 2nd Ed., PTR Prentice Hall, Upper Saddle River, Englewood Cliffs, NJ, 1999.

Maine, R.E. & Iliff, K.W. (1986). Identification of dynamic systems: theory and formulation. *NASA RF 1168*, June 1986.

Roskam, J. (1995) *Airplane Flight Dynamics and Automatic Flight controls*, DARcorporation, KS, 1995.

Soule, H.A. & Miller, M. P. (1934). The experimental determination of the moments of inertia of airplanes. *NACA Report 467*, 1934. Available: (http://naca.larc.nasa.gov/reports/1934/).

Hock, W. & Schittowski, K. (1983). A Comparative performance evaluation of 27 nonlinear programming codes. *Computing*, Vol. 30, p. 335, 1983.

Campa, G.; Gu, Y.; Seanor, B.; Napolitano, M. R.; Pollini, L. & Fravolini, M. L. (2007) Design And Flight Testing Of Nonlinear Formation Control Laws. *Control Engineering Practice*, pp 1077-1092, Vol. 15, Issue 9, September 2007.

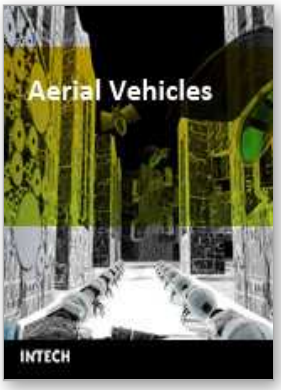

Aerial Vehicles

Edited by Thanh Mung Lam

ISBN 978-953-7619-41-1
Hard cover, 320 pages
Publisher InTech
Published online 01, January, 2009
Published in print edition January, 2009

This book contains 35 chapters written by experts in developing techniques for making aerial vehicles more intelligent, more reliable, more flexible in use, and safer in operation.It will also serve as an inspiration for further improvement of the design and application of aeral vehicles. The advanced techniques and research described here may also be applicable to other high-tech areas such as robotics, avionics, vetronics, and space.

InTech Europe
University Campus STeP Ri
Slavka Krautzeka 83/A
51000 Rijeka, Croatia
Phone: +385 (51) 770 447
Fax: +385 (51) 686 166
www.intechopen.com

InTech China
Unit 405, Office Block, Hotel Equatorial Shanghai
No.65, Yan An Road (West), Shanghai, 200040, China
中国上海市延安西路65号上海国际贵都大饭店办公楼405单元
Phone: +86-21-62489820
Fax: +86-21-62489821